ISSN 2075-3810 (Print), ISSN 2075-3829 (Online)

БІОФІЗИЧНИЙ ВІСНИК, 2026, Вип. 55 BIOPHYSICAL BULLETIN, 2026, Iss. 55

MOLECULAR BIOPHYSICS

Original article

https://doi.org/10.26565/2075-3810-2026-55-07

UDC 577.322:004.942:616.24-006.6

COMPUTATIONAL MODELING OF SELECTED PHYTOCHEMICALS FROM *Reevesia formosana*: MECHANISTIC INSIGHTS INTO THEIR POTENTIAL AGAINST LUNG CANCER

Hung Duc Nguyen

Faculty of Biology, Thai Nguyen University of Education, 24000, Thai Nguyen, Vietnam

e-mail: hungnd@tnue.edu.vn

Submitted December 10, 2025; Revised March 07, 2026;
Accepted March 16, 2026; Published June 25, 2026

Background: Lung cancer remains a dominant cause of cancer mortality, and impaired apoptosis mediated by anti-apoptotic Bcl-2 family proteins contributes to persistence and treatment resistance. Phytochemicals from *Reevesia formosana* display reported anti-NSCLC (Non-Small Cell Lung Cancer) activity, yet target-level mechanisms remain incompletely defined.

Objectives: To prioritize *Reevesia formosana* phytochemicals as putative Bcl-2 (PDB ID: 6GL8) inhibitors and to derive mechanistic insight through multiscale computation.

Materials and methods: Six phytochemicals and the reference Tivantinib were docked to 6GL8, and the top candidate (CPD1) was evaluated by 100 ns molecular dynamics simulations alongside Tivantinib. MMGBSA binding free energies were computed from 125 snapshots spanning 20-100 ns. ADMET properties were predicted using pkCSM. Frontier-orbital and global reactivity descriptors were obtained by DFT.

Results: Docking ranked CPD1 highest (-10.15 kcal/mol) relative to Tivantinib (-8.83 kcal/mol), with hydrogen bonding to Tyr108 and Arg129 and extensive pocket complementarity. MD trajectories indicated a more confined CPD1-6GL8 complex (RMSD mainly 0.18–0.22 nm) than Tivantinib-6GL8 (0.21–0.26 nm, occasional 0.27-0.28 nm), with comparable compactness (Rg of 1.44 nm) and bounded SASA. Hydrogen-bond counts supported intermittent polar anchoring for CPD1 (0-3) and higher early sampling for Tivantinib. MMGBSA favored CPD1 (ΔTOTAL -32.87 ± 4.28 kcal/mol) over Tivantinib (-17.27 ± 2.81 kcal/mol), supported by stronger ΔVDWAALS (-40.76 vs -31.34 kcal/mol) and a smaller ΔG_SOLV (20.28 vs 24.14 kcal/mol). ADMET prediction indicated high intestinal absorption with limited solubility, restricted BBB/CNS permeability, fewer CYP inhibition flags, and no hepatotoxicity alert for CPD1, while hERG II inhibition was flagged for both ligands. DFT showed similar EHOMO (eV) but a narrower ΔE (eV) and higher ω (eV) for CPD1 than for Tivantinib.

Conclusions: Integrated modeling prioritizes CPD1 as a Bcl-2-targeting scaffold for lung cancer-relevant studies, supporting structure-guided optimization and experimental verification.

KEY WORDS: ADMET; anti-apoptosis; Bcl-2; MMGBSA; molecular modeling; *Reevesia formosana*.

Cancer was a leading cause of death globally in 2020, responsible for nearly 10 million deaths, or about one in six total deaths, with major risk factors being lifestyle-related and infections, disproportionately affecting low- and middle-income countries. Among of those, lung cancer is a major global health issue, consistently the leading cause of cancer deaths

Citation: Nguyen HD. Computational modeling of selected phytochemicals from *Reevesia formosana*: mechanistic insights into their potential against lung cancer. Biophysical Bulletin. 2026;55:76–94. https://doi.org/10.26565/2075-3810-2026-55-07

worldwide, responsible for nearly 1.8 million deaths annually, driven primarily by tobacco but also by air pollution, with disparities seen globally [1]. The primary cause of lung cancer is smoking tobacco, responsible for 80-90% of cases, due to over 60 carcinogens in smoke, but other major factors include secondhand smoke, radon gas, asbestos, air pollution, and genetic predispositions, affecting both smokers and non-smokers [2]. Lung cancers are primarily divided into two main groups: Non-Small Cell Lung Cancer (NSCLC), which is the most common type (about 85%) and grows slower, and Small Cell Lung Cancer (SCLC), which is more aggressive and makes up about 15% of cases, with a third, much rarer category being lung carcinoid tumors [3]. In NSCLC, evasion of programmed cell death is frequently supported by dysregulation of apoptosis-regulatory networks, including increased activity of anti-apoptotic members of the Bcl-2 family, enabling survival of genetically compromised cells and contributing to treatment resistance. Bcl-2 is a key anti-apoptotic protein that helps cancer cells, including those in NSCLC, survive by preventing programmed cell death, often leading to chemotherapy resistance [4, 5]. Accordingly, therapeutic inhibition of anti-apoptotic Bcl-2 family proteins may re-establish apoptotic signaling and mitigate resistance to standard chemotherapy and radiotherapy in NSCLC.

Programmed cell death by apoptosis represents a tightly regulated biological pathway defined by characteristic morphological and biochemical hallmarks, including cell shrinkage, chromatin condensation, membrane blebbing, and caspase-driven proteolysis [6]. In many cancers, impaired mitochondrial apoptosis is closely linked to dysregulation of the Bcl-2 family, a network of pro- and anti-apoptotic regulators that controls mitochondrial outer membrane permeabilization and downstream caspase activation. Overexpression or functional dominance of anti-apoptotic members such as Bcl-2 contributes to apoptosis evasion and therapeutic resistance, supporting pharmacological blockade of Bcl-2 as a rational anticancer strategy [7]. Consequently, the central role of Bcl-2-mediated apoptotic blockade in cancer progression and drug resistance motivates the search for new, chemically diverse Bcl-2 inhibitors, for which natural products offer an especially rich and underexploited source of apoptosis-modulating scaffolds [8].

Plant-derived compounds are crucial in drug discovery, providing complex scaffolds for treatments like anticancer, highlighting their ongoing importance despite synthetic challenges, as they offer unique structures and often lower toxicity than purely synthetic counterparts, driving innovation in areas from oncology to neurology [9, 10]. Plant-derived compounds show significant promise in treating NSCLC by inhibiting cancer cell growth, inducing death, and modulating signaling pathways, often acting as adjuvants to enhance chemotherapy/targeted therapy effectiveness and overcome drug resistance, highlighting their potential to improve treatment outcomes and quality of life, though more clinical trials are needed [11, 12]. Building on this therapeutic potential, computational modeling provides a rational and resource-efficient framework to clarify how such phytochemicals engage molecular targets, prioritize candidates, and generate mechanistic hypotheses prior to extensive experimental validation. The mechanism of plant-derived compounds is unveiled computationally through a multi-stage process that integrates various bioinformatics and cheminformatics methods. These approaches streamline the traditional drug discovery pipeline, making it faster and more cost-effective than solely experimental methods [11, 13]. *Reevesia formosana* Sprague is highly cytotoxic, with its root, stem, and fruits containing potent anticancer compounds that showed significant activity against various cancer cell lines, making it a standout among many Formosan plants studied for their bioactivity. Previous study on this species led to the isolation of several phytochemicals with anti NSCLC activity against the NCI-H460 cancer cell line [14]. Despite these advances, the mechanistic underpinnings of their bioactivity, particularly within apoptosis-regulatory pathways, remain underexplored. Therefore, the aim of this study was to prioritize selected

phytochemicals from *R. formosana* as putative Bcl-2 (PDB ID: 6GL8) inhibitors and to gain mechanistic insight into their binding behavior using an integrated in silico approach, including molecular docking, molecular dynamics simulations, MMGBSA, ADMET prediction, and DFT-based electronic descriptors. The combined outputs support prioritization of these phytochemicals for subsequent experimental validation and structure-guided optimization in lung cancer-relevant models, while safety-related inferences remain provisional until confirmation through dedicated in vitro and in vivo investigations.

MATERIALS AND METHODS

Structural preparation of selected ligands

These selected phytochemical, including reevesioside J (CPD1), epi-reevesioside K (CPD2), reevesiterpenol C (CPD3), reevesiterpenol E (CPD4), strophanthidin (CPD5), oleanolic acid (CPD6), have molecular formulas of $C_{30}H_{44}O_8$, $C_{30}H_{38}O_{10}$, $C_{15}H_{20}O_4$, $C_{16}H_{16}O_5$, $C_{23}H_{32}O_6$, $C_{30}H_{48}O_3$, respectively, with molecular weights of 532.3036, 558.2465, 264.1362, 288.0998, 404.2199, 456.3603 *g/mol*. Tivantinib, possessing a molecular formula of $C_{23}H_{19}N_3O_2$ and a molecular weight of 369.1477 *g/mol*, was chosen as the positive control (Fig. 1).

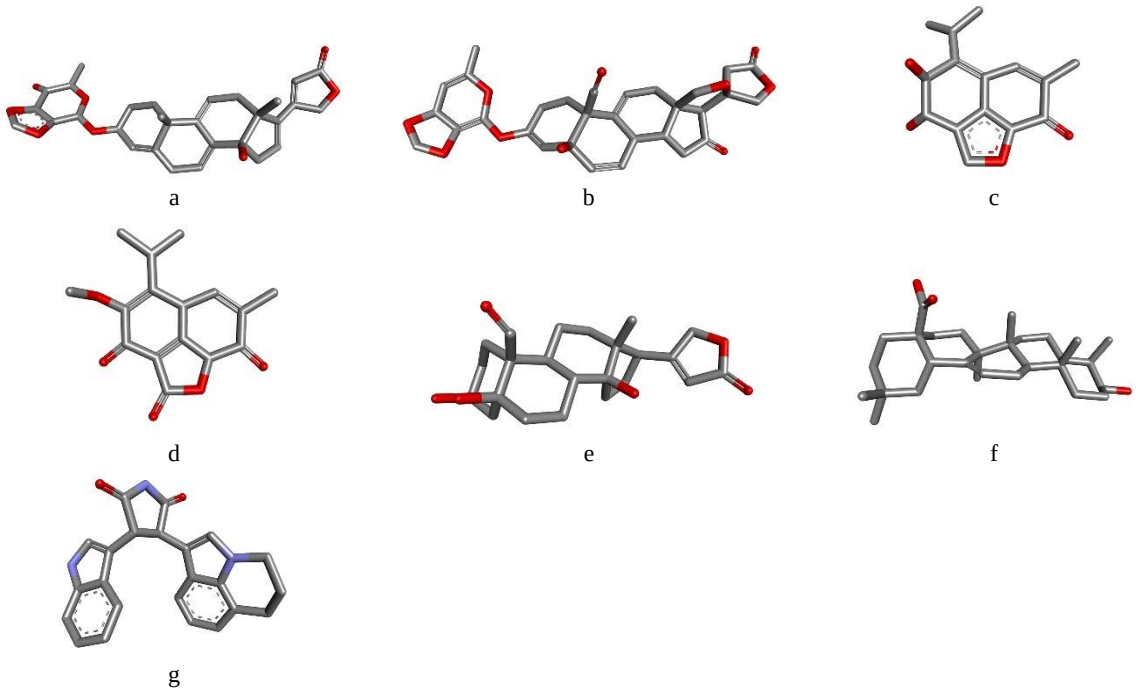

Fig. 1. 3D structures of selected phytochemicals. (a) CPD1; (b) CPD2; (c) CPD3; (d) CPD4; (e) CPD5; (f) CPD6; (g) Tivantinib.

Molecular docking study

Three-dimensional geometries of the selected ligands were constructed with BIOVIA Discovery Studio Visualizer and saved in PDB format. Polar hydrogen atoms were added, Gasteiger partial charges were assigned, and all rotatable bonds were treated as flexible for the docking procedure. The crystallographic structure of Bcl-2 (PDB ID: 6GL8) was retrieved from the RCSB Protein Data Bank in PDB format [15]. Non-protein entities (co-crystallized ligand and crystallographic waters) were removed to avoid bias in the binding site. The receptor was checked for incomplete residues/atoms and corrected when needed. Polar hydrogens were added, and Gasteiger partial charges were assigned to the receptor. The prepared receptor was saved in PDBQT format for docking. Ligand-protein docking was performed in AutoDock

Tools, using a grid with 60 points along each of the x, y, and z directions and a spacing of 0.375 Å. The grid was centered on the binding pocket of 6GL8, defined by coordinates x = 9.866 Å, y = 0.590 Å, and z = 16.717 Å. Conformational sampling employed the Lamarckian genetic algorithm, which enabled identification of low-energy binding modes and energetically favorable interaction patterns. For each ligand, the highest-ranked pose was subsequently examined in Discovery Studio Client 2024 and compared with the docking configuration of Tivantinib on the same Bcl-2 structure in order to assess similarities in binding mode and interaction profile [16].

Molecular dynamics simulation

Molecular dynamics simulations of the highest-ranked docking pose of the ligand in complex with the Bcl-2 protein (PDB ID: 6GL8) were performed for 100 ns using GROMACS 2024.4 [17]. Prior to the production stage, the protein structure was refined in Swiss-PdbViewer by reconstructing missing residues and atoms [17]. Force-field parameters compatible with the simulation were generated for the ligand using SwissParam [18]. The refined complex was inserted into a triclinic simulation box containing SPC water molecules and supplemented with 0.15 M NaCl to reproduce physiological ionic strength. Energy minimization was executed for 50,000 steps to reduce steric conflicts and stabilize electrostatic interactions. System equilibration employed a two-phase protocol, consisting of a 200 ps NVT stage followed by a 200 ps NPT stage, both maintained at 300 K and 1 bar. Production simulations were conducted in three independent replicas, each extending for 100 ns with a 2 fs integration timestep, and trajectory frames were stored every 10 ps. Trajectory analysis with Grace quantified root mean square deviation (RMSD), root mean square fluctuation (RMSF), radius of gyration (Rg), number of hydrogen bonds (H-bonds), and solvent-accessible surface area (SASA). Structural superimposition in UCSF Chimera 1.13.3 allowed assessment of conformational stability across all simulated complexes [19]. To evaluate interaction persistence, ligand orientations at 0 ns and 100 ns were aligned within the binding site, and the continuity of hydrogen bonding, van der Waals forces, and hydrophobic interactions throughout the 100 ns simulation was examined to provide insight into the durability and dynamical behavior of the complex.

Binding free energy calculation using MMGBSA

Binding free energy estimation for the CPD1-6GL8 and Tivantinib-6GL8 complexes was conducted with the gmx_MMPBSA workflow under the charmm36 force field. The polar term of solvation was evaluated using a generalized Born implicit-solvent formulation, whereas the non-polar contribution was derived from solvent-accessible surface area calculations. Calculations were performed on an ensemble of snapshots obtained from the molecular dynamics trajectories during the 20–100 ns window (80 ns total), comprising 125 evenly distributed frames sampled at 80 ps intervals. This trajectory-averaged strategy allowed quantitative comparison of the interaction energetics of the two ligands, thereby elucidating differences in relative binding affinity and complex stability across the analyzed simulation segment [20].

ADMET prediction

Assessment of ADMET attributes constitutes a fundamental component of preclinical screening, enabling early recognition of pharmacokinetic limitations and safety liabilities, reducing late-stage failure, and improving prioritization of candidates with favorable therapeutic potential. In the present work, the pkCSM platform was employed to predict the ADMET profiles of CPD1 and Tivantinib. pkCSM generates estimates using graph-based

molecular signatures, thereby supporting a structured evaluation of absorption, distribution, metabolism, excretion, and toxicity characteristics for the selected compounds [21].

Quantum DFT Analysis

Geometry optimisation of CPD1 and Tivantinib was executed in the ORCA quantum-chemistry package (v6.1.0). Starting conformations were generated in Avogadro, whereas molecular orbital inspection and associated electronic evaluations were performed in IboView (v20211019) [22–24]. Density functional theory calculations were carried out using the B3LYP exchange-correlation functional in combination with the 6-31G(d,p) basis set to obtain consistent electronic wavefunctions. Using the converged, fully optimised structures, quantum-chemical descriptors were computed, including the energies of the highest occupied molecular orbital (HOMO) and the lowest unoccupied molecular orbital (LUMO), the HOMO-LUMO energy gap (ΔE), chemical potential (μ), electronegativity (χ), global hardness (η), softness (σ), and electrophilicity index (ω). These indices were interpreted under the Koopmans' theorem framework to delineate electronic characteristics and infer the chemical reactivity of the investigated compounds [25, 26].

RESULTS AND DISCUSSION

Molecular docking analysis

Molecular docking assess how well potential drug molecules fit into a protein's binding site, predicting their binding affinity and pose, crucial for drug discovery to find potent inhibitors by ranking compounds based on scores and identifying key interactions with the target protein, often followed by more detailed molecular dynamics simulations for stability analysis. Before docking the ligands into 6GL8, protocol performance was assessed by re-docking the co-crystallized ligand (Fig. 2). The re-docked conformation closely matched the experimentally observed binding orientation, with an RMSD of 0.7540 Å, supporting adequacy of the docking parameters and search space definition. In docking validation, RMSD values below 2 Å are commonly regarded as indicative of acceptable pose reproduction and methodological reliability [27]. After validation, docked conformations were ranked by predicted binding score, where increasingly negative binding energies (kcal/mol) correspond to more favorable predicted binding.

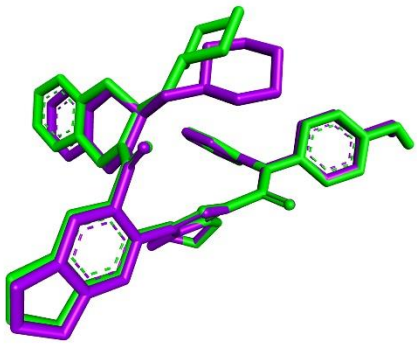

Fig. 2. The superimposition of the docked and native ligands within 6GL8 protein for validation of the molecular docking protocol (violet = native, green = docked).

As summarized in Table 1, docking-derived binding energies and residue-level contact patterns were evaluated for six phytochemical candidates (CPD1–CPD6) within a conserved pocket characterized by recurrent participation of Phe104, Tyr108, Asp111, Phe112, Gln118, Leu137, Ala149, and Phe153. Tivantinib served as the reference ligand under the same docking

protocol. Across all complexes, the interaction landscape reflected a combination of hydrogen bonding and short-range contact complementarity within an aromatic-aliphatic cavity enriched in Phe and Tyr side chains, with polar anchoring frequently involving Asp111 and Gln118.

Table 1. The interactions between the docked ligands and the protein 6GL8

Docked ligands	Binding energy (kcal/mol)	Hydrogen bond	Van der Waals force	Hydrophobic interaction
CPD1	-10.15	Tyr108, Arg129	Asp111, Phe112, Gln118, Thr132, Glu136, Leu137, Ala149	Phe104, Tyr108, Met115, Leu119, Val133, Phe153
CPD2	-9.25	-	Met115, Gln118, His120, Arg129, Thr132, Glu136, Arg146	Phe104, Tyr108, Leu119, Val133, Ala149, Phe153
CPD3	-6.64	-	Asp111, Gln118, Leu119, Val133, Glu152, Phe153	Phe104, Tyr108, Phe112, Met115, Leu137, Ala149
CPD4	-6.44	Gln118	Asp111, Glu114, Phe152	Phe104, Tyr108, Phe112, Met115, Leu119, Val133, Leu137, Ala149
CPD5	-6.87	Gln118	Tyr108, Asp111, Leu119, Arg129, Ala149, Glu152	Phe104, Phe112, Met115, Val133, Phe153
CPD6	-8.78	Asp111, Arg129	Phe104, Gln118, Thr132, Glu136, Leu137	Phe112, Met115, Leu119, Arg129, Val133, Phe153
Tivantinib	-8.83	Ala149	Asp111, Gln118, Leu137, Phe150, Glu152, Phe153	Phe104, Tyr108, Phe112, Met115, Leu119, Val133, Ala149

Within the selected ligands, predicted affinities spanned -10.15 to -6.44 kcal/mol. CPD1 exhibited the most favorable binding energy (-10.15 kcal/mol) and engaged the full set of canonical pocket residues (Phe104, Tyr108, Asp111, Phe112, Gln118, Leu137, Ala149, Phe153). In addition, CPD1 formed two hydrogen bonds involving Tyr108 and Arg129, consistent with a binding pose stabilized by both aromatic enclosure and directional polar constraints (Fig. 3a). CPD2 ranked second by docking score (-9.25 kcal/mol) and maintained contacts with key residues (Phe104, Tyr108, Gln118, Leu137, Ala149, Phe153), with additional proximity to Arg146. However, no hydrogen bond was annotated for CPD2, suggesting that the predicted stabilization may primarily arise from nonpolar packing and van der Waals complementarity rather than explicit polar locking. The selected receptor 6GL8 is a co-crystal structure of Bcl-2 bound to S55746, a selective BH3-mimetic that occupies the hydrophobic groove of Bcl-2. In the reported binding mode, S55746 forms a single hydrogen bond to the backbone carbonyl of Ala149 and is stabilized by extensive hydrophobic and van der Waals interactions within the BH3 groove [15]. Based on the deposited 6GL8 coordinates, residues

lining the S55746 pocket include Phe104, Tyr108, Asp111, Phe112, Met115, Gln118, Val133, Glu136, Leu137, Gly145, Arg146, Ala149, Glu152, and Phe153, defining a conserved aromatic-aliphatic cavity. Notably, CPD1 recapitulates multiple key groove contacts observed for S55746, including Phe104, Tyr108, Asp111, Phe112, Met115, Gln118, Val133, Glu136, Leu137, Ala149, and Phe153, supporting that CPD1 is positioned within the canonical BH3-binding groove similarly to a crystallographically validated Bcl-2 inhibitor, while exhibiting an alternative polar-anchoring pattern (Tyr108 and Arg129).

The reference compound Tivantinib yielded a binding energy of -8.83 kcal/mol, with contacts mapped to the core pocket residues (Phe104, Tyr108, Asp111, Phe112, Gln118, Leu137, Ala149, Phe153) and a hydrogen bond assigned to Ala149. CPD6 displayed a closely comparable affinity (-8.78 kcal/mol) and contacted Phe104, Asp111, Phe112, Gln118, Leu137, and Phe153, while the hydrogen-bond network involved Asp111 and Arg129. Notably, Ala149 did not appear among the CPD6 contact residues, indicating a slightly shifted occupancy within the pocket relative to Tivantinib, despite preservation of interactions around Asp111/Gln118 and the aromatic residues (Fig. 3b).

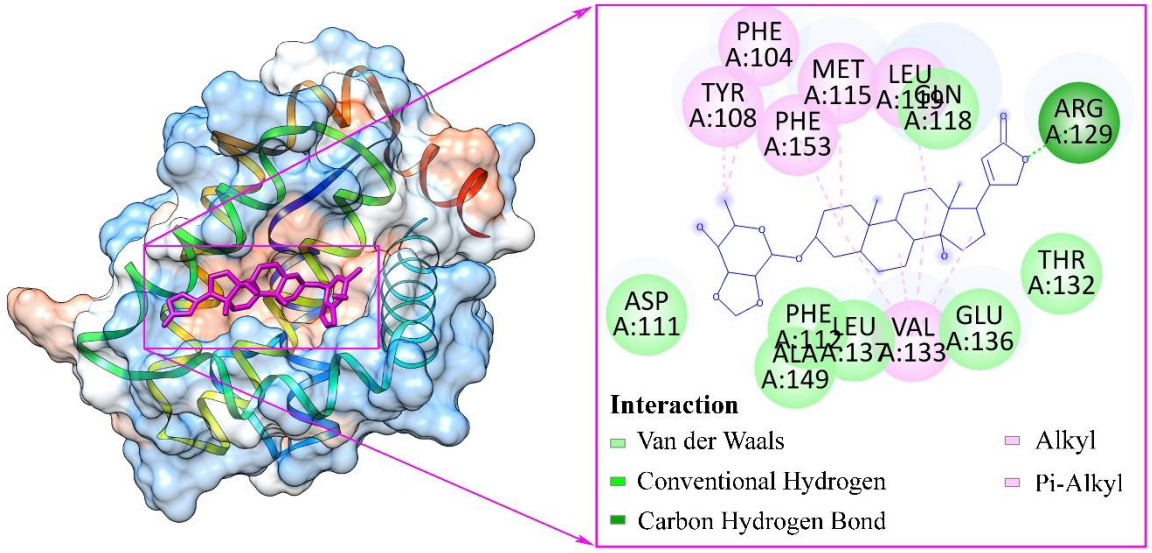

a

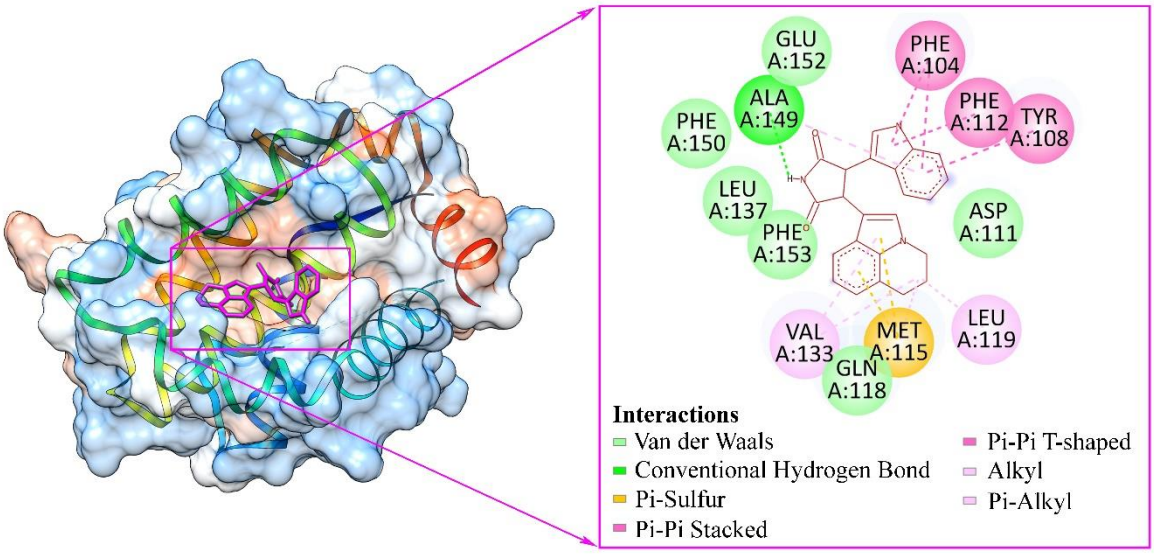

b

Fig. 3. Molecular docking model and 2D interaction diagram of CPD1 (a), and Tivantinib (b) with 6GL8 protein.

The remaining ligands showed more moderate predicted stabilization. CPD5 produced -6.87 kcal/mol and included a hydrogen bond to Gln118, alongside contacts with Phe104, Tyr108, Asp111, Phe112, Ala149, and Phe153. CPD3 (-6.64 kcal/mol) and CPD4 (-6.44 kcal/mol) both retained the canonical pocket residue set, yet CPD3 lacked annotated hydrogen bonding whereas CPD4 presented a single hydrogen bond to Gln118. Collectively, the dataset indicates that higher affinity within this series coincided with retention of the core pocket residues, supplemented in several cases by hydrogen-bond formation at Tyr108, Asp111, Gln118, Ala149, or Arg129. On the basis of docking, CPD1 and CPD2 outperformed Tivantinib, while CPD6 showed near-equivalent affinity. CPD1 was therefore advanced to molecular dynamics as the top-ranked scaffold, with CPD2 and CPD6 reserved for subsequent simulation-based validation.

Molecular dynamics simulations analysis

Molecular dynamics simulation represents a widely adopted approach in contemporary drug discovery, enabling time-resolved, atomistic characterization of ligand-target recognition. By propagating atomic trajectories under defined thermodynamic conditions, molecular dynamics elucidates conformational flexibility, binding-mode stability, and interaction energetics that inform mechanistic interpretation of molecular association. The resulting ensembles provide access to protein dynamical behavior, including transient pocket formation and allosteric communication, and delineate the influence of solvent structure and water-mediated contacts on affinity and selectivity. These capabilities facilitate rational lead optimization and can reduce reliance on extensive experimental iteration; however, integration with experimental validation remains essential to ensure translational reliability of computational predictions [28]. Integrating molecular docking with molecular dynamics provides an efficient structure-based workflow: docking rapidly screens binding poses and approximates affinity, whereas molecular dynamics evaluates time-dependent stability under conformational flexibility and solvent effects. This combination reduces false positives and improves lead optimization from initial hits to refined candidates [29]. Therefore, the evaluation systematically investigated RMSD, RMSF, Rg, H-bonds, and SASA metrics to determine the stability, flexibility, and solvent exposure of the CPD1-6GL8 and Tivantinib-6GL8 complexes throughout the simulation. Consequently, the total energy and potential energy values for the CPD1-6GL8 complex were found to be -227,502 kJ/mol and -282,584 kJ/mol, respectively. For the Tivantinib-6GL8 complex, the total energy and potential energy values were measured at -228,160 kJ/mol and -283,113 kJ/mol, respectively. The simulation system maintained equilibrium at a temperature of 300 K.

Root mean square deviation (RMSD) provides a time-resolved measure of structural departure from the starting reference after optimal superposition, and is routinely applied to evaluate equilibration behavior and overall conformational stability during molecular dynamics simulations [30]. Over the 100 ns trajectory, the CPD1-6GL8 complex exhibited an initial accommodation within the first several nanoseconds and subsequently remained largely confined, with RMSD values predominantly distributed around 0.18–0.22 nm (Fig. 4a). In contrast, the Tivantinib-6GL8 complex showed a comparable early regime but transitioned toward higher RMSD after approximately the first third of the simulation, fluctuating mainly around 0.21–0.26 nm with sporadic excursions approaching 0.27–0.28 nm. The absence of abrupt jumps suggests preservation of the folded framework in both systems; however, the consistently lower RMSD envelope observed for CPD1 indicates tighter structural confinement relative to the reference ligand under the simulated conditions.

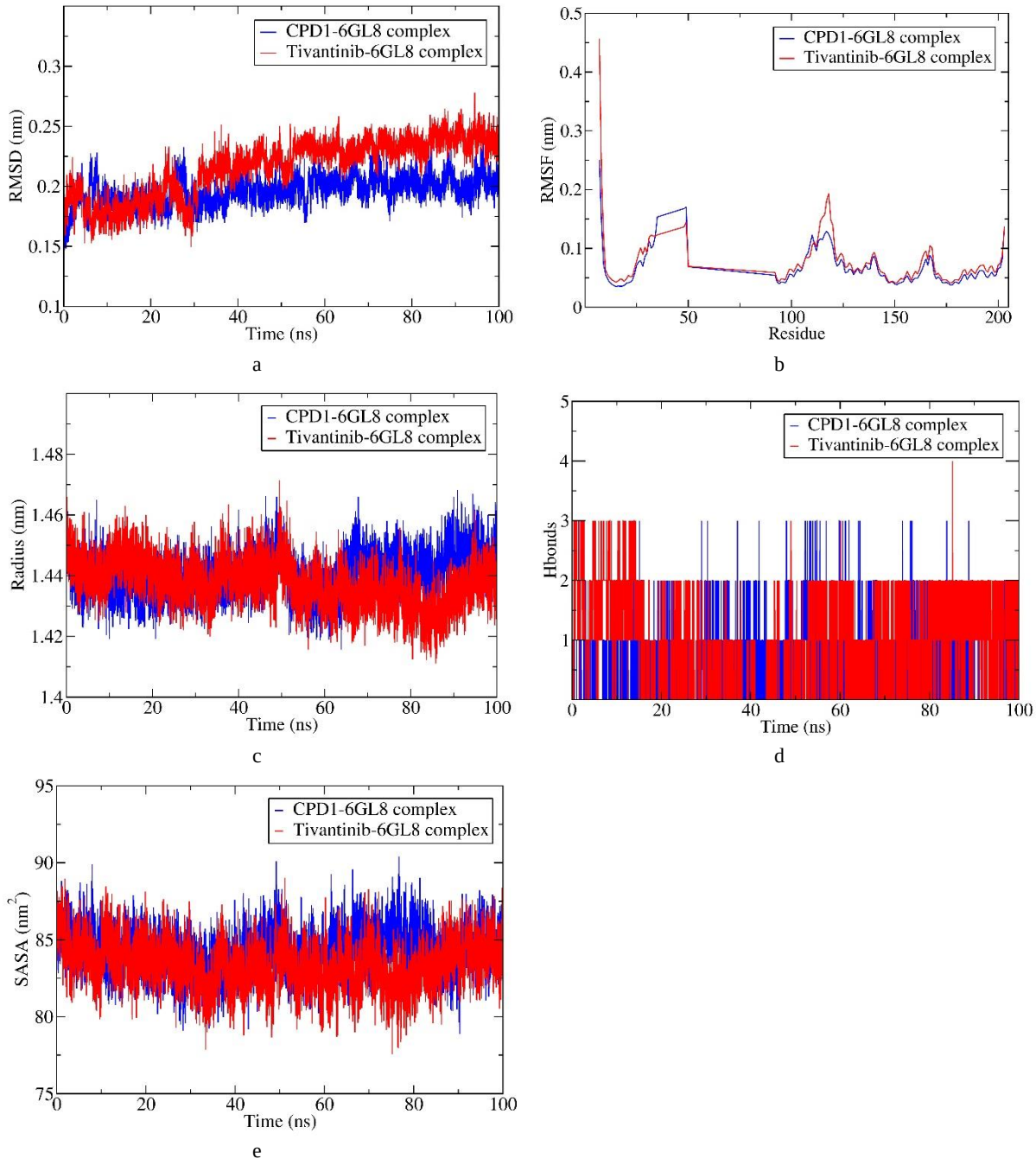

Fig. 4. Results of MD simulation for the bindings of CPD1 (blue) and Tivantinib (red) with 6GL8 protein. (a) RMSD, (b) RMSF, (c) Rg, (d) H-bonds, and (e) SASA.

Root mean square fluctuation (RMSF) quantifies residue-wise mobility around the time-averaged position, enabling localization of flexible segments and comparatively rigid secondary-structure elements [31]. After recalculation of RMSF on a residue basis from the 100 ns trajectories, both complexes displayed the expected non-uniform fluctuation pattern across 6GL8, with the highest mobility localized at the N-terminal region and several additional local maxima along the sequence (Fig. 4b). The largest fluctuation was observed at Gly7 in both systems, reaching 0.249 nm for CPD1-6GL8 and 0.456 nm for Tivantinib-6GL8, indicating markedly greater terminal mobility in the Tivantinib-bound complex. Beyond the N-terminus, local fluctuation peaks were evident in the regions around residues 24–35, 48–50, and most prominently 114–120, with Tivantinib generally producing higher RMSF values than CPD1. In

particular, the 114–120 segment reached approximately 0.116–0.129 nm in the CPD1-6GL8 complex, whereas the corresponding values in the Tivantinib-6GL8 complex increased to about 0.147–0.193 nm. Across most of the remaining structured residues, RMSF values remained relatively low, predominantly within 0.04–0.09 nm for both systems, consistent with preservation of the overall protein fold during simulation. Collectively, the corrected residue-wise RMSF analysis indicates that the Tivantinib-bound complex undergoes somewhat greater local mobility than the CPD1-bound complex, whereas CPD1 maintains comparably lower fluctuations over much of the 6GL8 structure, supporting slightly greater dynamic stabilization under the simulated conditions. Because the crystallographic structure of 6GL8 contains unresolved segments, residue numbering in the RMSF plot follows the native PDB indexing, and missing regions are absent from the profile rather than analyzed as continuous residues.

The radius of gyration (Rg) reflects mass-weighted compactness of the protein assembly and is commonly monitored to detect expansion or compaction events during simulation. As shown in Figure 4c, both complexes maintained Rg within a narrow band centered near 1.44 nm, indicating sustained global compactness without signatures of unfolding. CPD1-6GL8 fluctuated approximately within 1.42–1.47 nm, with a modest upward tendency after 65 ns toward the 1.45–1.46 nm region. Tivantinib-6GL8 occupied a similar interval but exhibited a clearer transient compaction during 75–85 ns, with minima approaching 1.41–1.42 nm. These patterns indicate stable global architecture for 6GL8 in both ligand-bound states, with small ligand-dependent shifts in compactness.

In molecular dynamics, the number of hydrogen bonds (H-bonds) indicates the strength, stability, and structural integrity of interactions, showing how many temporary links form between molecules over time; a higher count often means stronger binding/structure, while tracking changes reveals dynamic processes like protein folding, binding/unbinding, or solvent effects, influencing overall system stability and function [32]. Across the 100 ns simulation (Fig. 4d), the CPD1-6GL8 complex exhibited H-bonds values primarily between 0 and 2, interspersed with short-lived events reaching 3. The Tivantinib-6GL8 complex displayed a broader distribution, commonly populating 1–2 and frequently sampling 3 during the early segment of the trajectory, with an isolated spike reaching 4 near the late stage. Collectively, the profiles indicate that polar contacts persisted intermittently in both systems; the reference ligand showed a higher early-time propensity for multiple H-bonds, whereas CPD1 maintained stability despite a lower upper bound for most of the trajectory.

Solvent-accessible surface area (SASA) reports the extent of solvent exposure and is sensitive to changes in packing and conformational breathing motions. The SASA traces for both complexes remained within a confined range throughout 100 ns, without sustained drift indicative of progressive expansion or collapse (Fig. 4e). CPD1-6GL8 fluctuated approximately within 79–90 nm² and showed a modest elevation during 60-85 ns relative to earlier frames, consistent with slightly increased solvent exposure. Tivantinib-6GL8 spanned roughly 78–89 nm² and displayed comparatively lower SASA during the same window, suggesting transiently reduced exposure and marginally tighter packing. The broadly similar oscillatory behavior across both systems supports stable solvent-exposed surface properties over the analyzed trajectory.

Collectively, the integrated molecular dynamics descriptors delineate the dynamic stability and binding behavior of the CPD1-6GL8 and Tivantinib-6GL8 complexes, underscoring the contribution of 6GL8 pocket dynamics to ligand accommodation. The CPD1-6GL8 system exhibited a generally lower RMSD envelope with comparable compactness and controlled residue-level mobility in the Gly7-Gly203 region, supporting a slightly more stable association than the Tivantinib-6GL8 complex under identical conditions. These observations indicate that CPD1 can sustain persistent binding within the 6GL8 site and merits prioritization as a promising alternative scaffold for further investigation.

MMGBSA calculation

MMGBSA (Molecular Mechanics/Generalized Born Surface Area) is a fast, efficient computational method in drug discovery that estimates ligand-receptor binding free energy by combining molecular mechanics with implicit solvation models, analyzing snapshots from molecular dynamics) to score potential drug candidates, rank binding poses, and predict relative affinities, helping to filter promising compounds by breaking down energy into gas-phase, polar solvation, and nonpolar contributions. It's a powerful tool for virtual screening and lead optimization, offering a good balance between accuracy and computational cost compared to more rigorous methods [33]. Binding free energies of the CPD1-6GL8 and Tivantinib-6GL8 complexes were quantified using the MMGBSA scheme, where the binding term is defined as ΔG_bind = G_complex - (G_receptor + G_ligand). Although ΔG_bind can be written in the thermodynamic form ΔH - TΔS, omission of configurational entropy yields an enthalpy-weighted metric that remains informative for relative ranking when both ligands are evaluated under the same trajectory sampling and energy model. Energy decomposition was used to resolve the balance between gas-phase interactions (ΔG_GAS = ΔVDWAALS + ΔEEL) and solvation contributions (ΔG_SOLV = ΔEGB + ΔESURF), enabling interpretation of the dominant stabilization factors.

Table 2. Free energy of binding obtained using MMGBSA calculations

Energy Component	Average (kcal/mol)		Standard Deviation	
	CPD1-6GL8	Tivantinib-6GL8	CPD1-6GL8	Tivantinib-6GL8
ΔVDWAΔALS	-40.76	-31.34	3.62	2.78
ΔEEL	-12.38	-10.07	8.53	6.05
ΔEGB	25.22	28.45	7.93	4.72
ΔESURF	-4.93	-4.31	0.51	0.29
ΔGGAS	-53.15	-41.41	10.46	6.19
ΔGSOLV	20.28	24.14	7.55	4.57
ΔTOTAL	-32.87	-17.27	4.28	2.81

Consistent with the docking prioritization of CPD1 and the subsequent dynamics indicating tighter structural confinement, MMGBSA analysis produced negative total binding free energies for both complexes, with a pronounced advantage for CPD1. As detailed in Table 2, the mean ΔTOTAL reached -32.87 ± 4.28 kcal/mol for CPD1-6GL8, compared with -17.27 ± 2.81 kcal/mol for Tivantinib-6GL8, corresponding to a 15.60 kcal/mol more favorable estimate for CPD1. The larger dispersion for CPD1 suggests broader energetic sampling across the trajectory, yet the mean difference remains substantial relative to the reported standard deviations. The enhanced affinity of CPD1 is primarily explained by stronger gas-phase interactions. The gas-phase term was ΔG_GAS = -53.15 ± 10.46 kcal/mol for CPD1, whereas Tivantinib yielded -41.41 ± 6.19 kcal/mol. This gap is driven mainly by van der Waals stabilization, with ΔVDWAALS = -40.76 ± 3.62 kcal/mol for CPD1 versus -31.34 ± 2.78 kcal/mol for Tivantinib, indicating tighter short-range packing and shape complementarity in the CPD1-bound state. This pattern aligns with the docking contact map that placed CPD1 deeply within an aromatic-aliphatic cavity enriched in Phe/Tyr side chains and reported

extensive nonpolar contacts (Phe104, Tyr108, Met115, Leu119, Val133, Phe153) together with proximity to canonical pocket residues. Electrostatic interactions contribute additional stabilization in both systems and modestly favor CPD1 (ΔEEL = -12.38 ± 8.53 kcal/mol) over Tivantinib (-10.07 ± 6.05 kcal/mol). The comparatively higher variability of ΔEEL relative to ΔVDWAALS is compatible with time-dependent rearrangements of polar contacts during dynamics, particularly given that hydrogen-bond occupancy was intermittent over the 100 ns trajectories. Solvation effects oppose binding for both ligands, with ΔG_SOLV = 20.28 ± 7.55 kcal/mol for CPD1 and 24.14 ± 4.57 kcal/mol for Tivantinib. The unfavorable solvation term is dominated by the polar GB component (ΔEGB = 25.22 ± 7.93 kcal/mol for CPD1; 28.45 ± 4.72 kcal/mol for Tivantinib), whereas the nonpolar surface contribution provides a smaller favorable offset (ΔESURF = -4.93 ± 0.51 kcal/mol for CPD1; -4.31 ± 0.29 kcal/mol for Tivantinib). Therefore, beyond stronger gas-phase attraction, CPD1 also experiences a reduced desolvation penalty, which further shifts ΔTOTAL toward more favorable values. This solvation profile is congruent with the dynamics-derived picture of stable pocket accommodation without sustained expansion of solvent exposure, as SASA remained within a narrow range for both systems, supporting comparable global solvation environments while permitting ligand-specific differences in local desolvation costs.

Taken together, the MMGBSA decomposition indicates that the superior binding estimate for CPD1-6GL8 originates chiefly from more favorable van der Waals interactions and a lower polar solvation penalty, with electrostatics contributing additional but secondary stabilization. These energetic findings reinforce the docking outcome in which CPD1 achieved the best score and maintained canonical pocket residue engagement, and they are compatible with the molecular dynamics observations of a lower RMSD envelope and sustained complex stability under the simulated conditions.

ADMET prediction analysis

ADMET prediction in drug design uses computational models to estimate a compound's Absorption, Distribution, Metabolism, Excretion, and Toxicity early on, acting as a crucial filter to identify drug-like molecules, reduce late-stage failures, cut costs, and speed up development by predicting if a potential drug will work in the body and won't be harmful before expensive experiments. Thus, in silico ADMET profiling was conducted to characterize the predicted pharmacokinetic behavior and safety-relevant alerts of CPD1 in relation to the reference ligand Tivantinib, with descriptors organized across absorption, distribution, metabolism, excretion, and toxicity [34]. The resulting comparative profile supports prioritization decisions following docking and molecular dynamics analyses by highlighting parameters that may influence exposure, transporter liability, metabolic interaction potential, and toxicity risk. Predicted ADMET descriptors for CPD1 and Tivantinib are summarized in Table 3.

Across absorption metrics, both ligands exhibit limited predicted aqueous solubility, with water solubility values of -4.838 log mol/L for CPD1 and -4.405 log mol/L for Tivantinib, indicating similarly constrained dissolution and a modest solubility advantage for Tivantinib. In contrast, epithelial transport indices favor CPD1, as reflected by higher Caco-2 permeability (1.42 vs 1.122 log Papp in 10^{-6} cm/s) and higher predicted human intestinal absorption (98.498% vs 94.761% absorbed). Predicted skin permeability is comparable, with slightly more permissive dermal permeation for Tivantinib (-3.221 log Kp) relative to CPD1 (-3.441 log Kp). Transporter annotations indicate shared involvement with P-glycoprotein: both compounds are predicted to be P-glycoprotein substrates and to inhibit P-glycoprotein I and P-glycoprotein II, suggesting potential for efflux-related modulation of exposure and interaction risk in barrier tissues [35].

Table 3. Predicted ADMET properties of CPD1 and Tivantinib

ADMET properties	Unit	CPD1	Tivantinib
Water Solubility	(Log mol/L)	-4.838	-4.405
Caco2 permeability	(Log Papp in 10-6 cm/s)	1.42	1.122
Intestinal absorption (Human)	(% Absorbed)	98.498	94.761
Skin permeability	(Log Kp)	-3.441	-3.221
P-glycoprotein substrate	Yes/No	Yes	Yes
P-glycoprotein I inhibitor	Yes/No	Yes	Yes
P-glycoprotein II inhibitor	Yes/No	Yes	Yes
VDss	(Log L/kg)	0.21	-0.243
Fraction unbound (human)	(Fu)	0.234	0.046
BBB permeability	(Log BB)	-0.783	0.013
CNS permeability	(Log PS)	-3.253	-1.741
CYP2D6 substrate	Yes/No	No	No
CYP3A4 substrate	Yes/No	Yes	Yes
CYP1A2 inhibitor	Yes/No	No	Yes
CYP2C19 inhibitor	Yes/No	No	Yes
CYP2C9 inhibitor	Yes/No	No	No
CYP2D6 inhibitor	Yes/No	No	No
CYP3A4 inhibitor	Yes/No	No	Yes
Total clearance	(Log ml/min/kg)	0.361	0.458
Renal OCT2 substrate	Yes/No	No	No
AMES toxicity	Yes/No	No	No
Max. tolerated dose (human)	(Log mg/kg/day)	-1.139	0.578
hERG I inhibitor	Yes/No	No	No
hERG II inhibitor	Yes/No	Yes	Yes
Oral rat acute toxicity (LD50)	(mol/kg)	2.474	2.774
Oral rat chronic toxicity (LOAEL)	(Log mg/kg_bw/day)	1.496	2.22
Hepatotoxicity	Yes/No	No	Yes
Skin sensation	Yes/No	No	No
Tetrahymena pyriformis toxicity	(Log ug/L)	0.291	0.462
Minnow toxicity	(Log mM)	0.505	0.65

Distribution parameters differentiate systemic disposition and central exposure. The predicted steady-state volume of distribution is higher for CPD1 (VDss = 0.21 log L/kg) than for Tivantinib (-0.243 log L/kg), consistent with a greater modeled tendency toward tissue distribution for CPD1. Plasma protein binding is predicted to be weaker for CPD1, as indicated by a larger fraction unbound (Fu) (0.234) compared with Tivantinib (0.046), which may increase free-drug availability in circulation under the model assumptions. Central penetration estimates diverge: BBB permeability (log BB) is -0.783 for CPD1 and 0.013 for Tivantinib, while CNS permeability (log PS) is -3.253 for CPD1 and -1.741 for Tivantinib. These values imply more restricted brain and CNS exposure for CPD1 relative to Tivantinib within the same prediction framework [36].

The metabolism profile indicates shared CYP substrate behavior with notable differences in inhibitory potential. Neither compound is categorized as a CYP2D6 substrate. Both ligands are predicted CYP3A4 substrates, consistent with CYP3A4-mediated metabolic involvement. Inhibition flags separate the profiles: CPD1 is predicted negative for CYP1A2, CYP2C19, and CYP3A4 inhibition, whereas Tivantinib is predicted positive for CYP1A2 inhibitor, CYP2C19 inhibitor, and CYP3A4 inhibitor status. Both ligands are predicted negative for CYP2C9 inhibitor and CYP2D6 inhibitor status [37]. Overall, CPD1 presents fewer predicted CYP inhibition liabilities than Tivantinib in the current output.

For excretion, predicted total clearance is lower for CPD1 (0.361 log ml/min/kg) than for Tivantinib (0.458 log ml/min/kg), suggesting slower modeled elimination for CPD1. Renal OCT2 substrate status is negative for both compounds, indicating no OCT2-associated designation under the applied predictor.

Toxicity endpoints show a mixed set of shared and divergent alerts. Both ligands are predicted AMES-negative and hERG I inhibitor-negative, while hERG II inhibition is flagged for both, indicating a common cardiac electrophysiology concern that warrants attention in subsequent validation. A clinically relevant separation appears for hepatotoxicity, predicted negative for CPD1 and positive for Tivantinib. Skin sensitization is predicted negative for both. Quantitative toxicity indices favor Tivantinib in the same predictive context: the maximum tolerated dose (human) is -1.139 log mg/kg/day for CPD1 versus 0.578 for Tivantinib; oral rat acute toxicity (LD50) is 2.474 mol/kg for CPD1 versus 2.774 mol/kg for Tivantinib; and oral rat chronic toxicity (LOAEL) is 1.496 log mg/kg_bw/day for CPD1 versus 2.22 for Tivantinib. Ecotoxicity-associated estimates are higher for Tivantinib than CPD1, including *Tetrahymena pyriformis* toxicity (0.462 vs 0.291 log μg/L) and minnow toxicity (0.65 vs 0.505 log mM).

Collectively, the ADMET profile indicates that CPD1 combines high predicted intestinal absorption and higher Caco-2 permeability with lower predicted solubility, shared P-glycoprotein involvement, and reduced BBB/CNS penetration relative to Tivantinib. The metabolic pattern suggests lower CYP inhibition propensity for CPD1, whereas Tivantinib carries multiple inhibitory flags (CYP1A2, CYP2C19, CYP3A4). Safety-relevant predictions highlight a hepatotoxicity alert for Tivantinib but not for CPD1, while hERG II inhibition remains a shared liability. These features complement the stronger interaction energetics observed for CPD1 in MMGBSA analysis and support its prioritization, with solubility constraints and cardiac-related alerts representing key aspects for further experimental assessment.

DFT calculations

Density Functional Theory (DFT) calculations are used in drug design to find the most stable, lowest-energy three-dimensional arrangement of atoms in a molecule, thereby optimizing its geometric coordinates. This optimized structure is crucial because a drug's efficacy and interaction with a biological target depend heavily on its precise shape and

electronic properties. Quantum chemical analysis using DFT was performed after the classical modeling stage to describe the electronic structure and reactivity-associated tendencies of CPD1 in comparison with the reference ligand Tivantinib. The computed descriptors included EHOMO (eV), ELUMO (eV), ΔE (eV), μ (eV), χ (eV), η (eV), σ (eV-1), and ω (eV), which jointly summarize frontier-orbital energetics, resistance to charge redistribution, and electrophilic character. In this context, EHOMO (eV) reflects electron-donation propensity, whereas ELUMO (eV) indicates electron-acceptance capability; ΔE (eV), defined as ELUMO (eV) - EHOMO (eV), serves as an index of electronic stability versus chemical responsiveness. DFT descriptors for CPD1 and Tivantinib are detailed in Table 4.

Table 4. DFT calculations for CPD1 and Tivantinib

Molecule	**EHOMO (eV)**	**ELUMO (eV)**	**ΔE (eV)**	**μ (eV)**	**χ (eV)**	**η (eV)**	**σ (eV^{-1})**	**ω (eV)**
CPD1	-7.4261	-3.7620	3.6641	-5.5941	5.5941	1.8321	0.5458	8.5405
Tivantinib	-7.4231	2.9976	10.4207	-2.2128	2.2128	5.2104	0.1919	0.4699

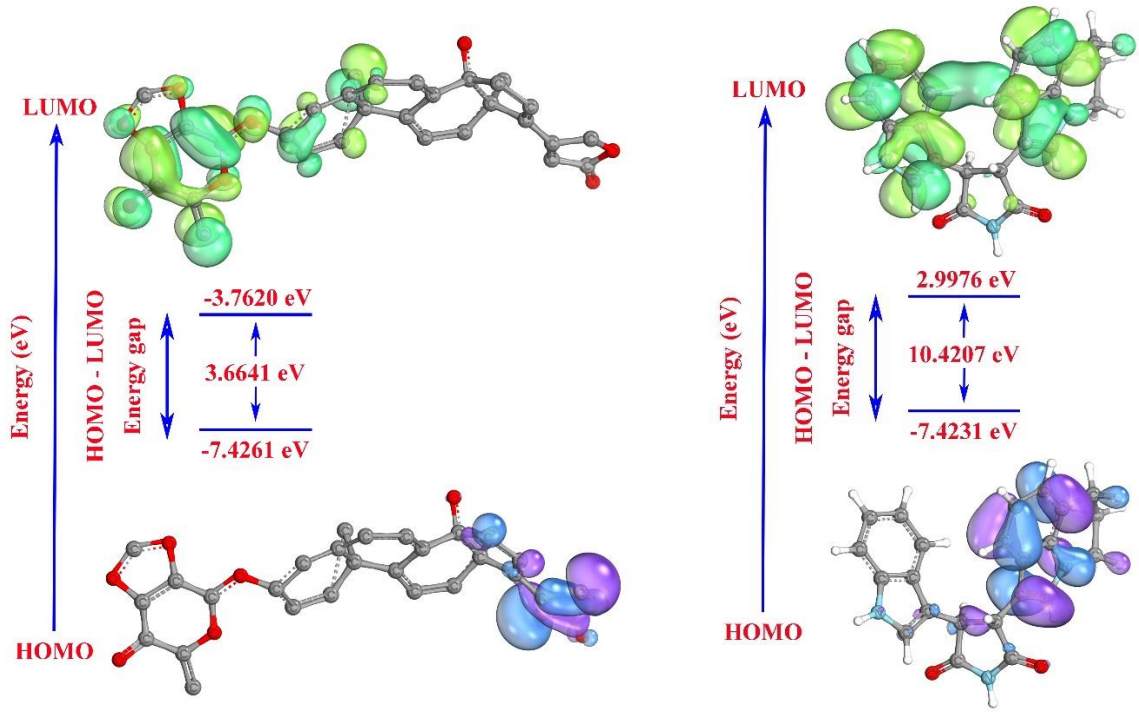

a b

Fig. 5. HOMO and LUMO surface diagrams of CPD1 (a) and Tivantinib (b).

The frontier-orbital energies indicate similar donor levels but strongly different acceptor levels. EHOMO (eV) for CPD1 is -7.4261, closely matching Tivantinib (-7.4231), suggesting comparable intrinsic electron-donating capability under the same calculation conditions. In contrast, ELUMO (eV) differs markedly, with CPD1 presenting a low-lying acceptor orbital (-3.7620) whereas Tivantinib exhibits a positive ELUMO (eV) (2.9976). As a direct consequence, CPD1 displays a substantially smaller ΔE (eV) (3.6641) than Tivantinib (10.4207). The reduced ΔE (eV) for CPD1 is consistent with increased electronic polarizability

and greater readiness for charge transfer, while the wide gap for Tivantinib is compatible with enhanced frontier-orbital stability and lower electronic responsiveness. Global reactivity descriptors further distinguish the two ligands. CPD1 shows higher χ (eV) (5.5941) than Tivantinib (2.2128), indicating stronger electron-attracting character within this DFT dataset. The corresponding μ (eV) values follow the expected inverse relationship with χ (eV), with CPD1 exhibiting a more negative chemical potential (-5.5941) relative to Tivantinib (-2.2128), implying a stronger thermodynamic tendency toward electron uptake. Electronic resistance to deformation, quantified by η (eV), is lower for CPD1 (1.8321) than for Tivantinib (5.2104), and the reciprocal descriptor σ (eV-1) is therefore higher for CPD1 (0.5458) than for Tivantinib (0.1919). This pairing supports greater softness and lower hardness for CPD1, consistent with the smaller ΔE (eV) and the associated capacity for charge redistribution (Fig. 5).

The electrophilic character, measured by ω (eV), shows the most pronounced separation: CPD1 has an electrophilicity index of 8.5405, whereas Tivantinib shows 0.4699. The markedly higher ω (eV) for CPD1 indicates stronger electrophilic strength according to the computed descriptors, in agreement with the combined pattern of higher χ (eV) and lower η (eV).

Overall, the DFT profile characterizes CPD1 as electronically softer and more electrophilic than Tivantinib, while maintaining a comparable donor orbital level as reflected by near-identical EHOMO (eV) values.

Despite the value of in silico screening for identifying prioritized candidates, experimental confirmation remains indispensable for establishing the robustness and translational relevance of the present predictions. No laboratory validation was conducted because of limited access to appropriate instrumentation and facilities. Subsequent work should therefore emphasize systematic in vitro and in vivo evaluation of CPD1, including target-engagement assays and biological model studies to delineate pharmacological efficacy alongside safety-relevant endpoints. The absence of experimental datasets, together with the lack of dedicated assessment of potential unintended covalent inhibition, constitutes a key limitation of the current investigation. If CPD1 demonstrates favorable performance in preclinical testing, progression toward clinically oriented studies may be justified. Overall, the current computational evidence provides a mechanistic basis that can guide rational follow-up experiments and support continued development toward therapeutic application.

CONCLUSIONS

This study integrated docking, molecular dynamics, MMGBSA, ADMET prediction, and DFT descriptors to examine *Reevesia formosana* phytochemicals as potential lung cancer-relevant inhibitors through interaction with the Bcl-2 protein (6GL8). CPD1 consistently emerged as the leading scaffold, exhibiting the most favorable docking profile within the conserved pocket, supported by hydrogen-bond anchoring and extensive short-range complementarity with key residues. Molecular dynamics indicated a more confined and persistent bound state for CPD1 relative to Tivantinib, consistent with sustained pocket accommodation under solvated conditions. MMGBSA energy decomposition further supported stronger association for CPD1, dominated by enhanced van der Waals stabilization with supportive electrostatics and a comparatively reduced solvation penalty. ADMET profiling suggested high oral absorption potential but limited aqueous solubility, shared P-glycoprotein liability, restricted central exposure, and fewer predicted CYP inhibition alerts for CPD1 than for Tivantinib; a hepatotoxicity alert was predicted for Tivantinib but not for CPD1, whereas a shared hERG II signal warrants caution. DFT analysis characterized CPD1 as electronically softer and more electrophilic than the reference, consistent with greater charge-redistribution propensity. Collectively, the convergent evidence prioritizes CPD1 for subsequent optimization

and experimental validation, with emphasis on solubility improvement and cardiotoxicity-focused risk assessment.

CONFLICT OF INTEREST

The authors declare that there is no conflict of interest.

Author's ORCID ID

Hung Duc Nguyen http://www.orcid.org/0000-0002-5764-1242

REFERENCES

1. Bray F, Laversanne M, Sung H, Ferlay J, Siegel RL, Soerjomataram I, et al. Global cancer statistics 2022: GLOBOCAN estimates of incidence and mortality worldwide for 36 cancers in 185 countries. CA: Cancer J Clin. 2024;74(3):229–63. https://doi.org/10.3322/caac.21834
2. Zou K, Sun P, Huang H, Zhuo H, Qie R, Xie Y, et al. Etiology of lung cancer: Evidence from epidemiologic studies. J Natl Cancer Cent. 2022;2(4):216–25. https://doi.org/10.1016/j.jncc.2022.09.004
3. Relli V, Trerotola M, Guerra E, Alberti S. Abandoning the notion of non-small cell lung cancer. Trends Mol Med. 2019;25(7):585–94. https://doi.org/10.1016/j.molmed.2019.04.012
4. Jiang S-X, Sato Y, Kuwao S, Kameya T. Expression of bcl-2 oncogene protein is prevalent in small cell lung carcinomas. J Pathol. 1995;177(2):135–8. https://doi.org/10.1002/path.1711770206
5. Qian S, Wei Z, Yang W, Huang J, Yang Y, Wang J. The role of BCL-2 family proteins in regulating apoptosis and cancer therapy. Front Oncol. 2022;12:985363. https://doi.org/10.3389/fonc.2022.985363
6. Mustafa M, Ahmad R, Tantry IQ, Ahmad W, Siddiqui S, Alam M, et al. Apoptosis: A comprehensive overview of signaling pathways, morphological changes, and physiological significance and therapeutic implications. Cells 2024;13(22):1838. https://doi.org/10.3390/cells13221838
7. Montero J, Haq R. Adapted to survive: Targeting cancer cells with BH3 mimetics. Cancer Discov. 2022;12(5):1217–32. https://doi.org/10.1158/2159-8290.CD-21-1334
8. Hassig CA, Zeng F-Y, Kung P, Kiankarimi M, Kim S, Diaz PW, et al. Ultra-high-throughput screening of natural product extracts to identify proapoptotic inhibitors of Bcl-2 family proteins. SLAS Discov. 2014;19(8):1201–11. https://doi.org/10.1177/1087057114536227
9. Shah U, Shah R, Acharya S, Acharya N. Novel anticancer agents from plant sources. Chin J Nat Med. 2013;11(1):16–23. https://doi.org/10.1016/S1875-5364(13)60002-3
10. Chihomvu P, Ganesan A, Gibbons S, Woollard K, Hayes MA. Phytochemicals in drug discovery-A confluence of tradition and innovation. Int J Mol Sci. 2024;25(16):8792. https://doi.org/10.3390/ijms25168792
11. Yang Y, Wang H, Xue Q, Peng W, Zhou Q. New advances of natural products in non-small cell lung cancer: From mechanisms to therapies. J Ethnopharmacol. 2025;346:119636. https://doi.org/10.1016/j.jep.2025.119636
12. Wei J, Yan Y, Chen X, Qian L, Zeng S, Li Z, et al. The roles of plant-derived triptolide on non-small cell lung cancer. Oncol Res. 2019;27(7):849-58. https://doi.org/10.3727/096504018X15447833065047
13. Othman ZK, Ahmed MM, Kasimieh O, Musa SS, Branda F, Cue EG, et al. Artificial intelligence for natural product drug discovery and development: current landscape, applications, and future directions. Intell Med. 2025;12:100316. https://doi.org/10.1016/j.ibmed.2025.100316
14. Hsiao PY, Lee SJ, Chen IS, Hsu HY, Chang HS. Cytotoxic cardenolides and sesquiterpenoids from the fruits of Reevesia formosana. Phytochemistry. 2016;130:282-90. https://doi.org/10.1016/j.phytochem.2016.06.009
15. Casara P, Davidson J, Claperon A, Toumelin-Braizat G Le, Vogler M, Bruno A, et al. S55746 is a novel orally active BCL2 selective and potent inhibitor that impairs hematological tumor growth. Oncotarget. 2018;9(28):20075–88. https://doi.org/10.18632/oncotarget.24744
16. Nguyen HD. DFT and molecular modelling reveal the mechanism of action of selected alkaloids as anti-colorectal cancer agents targeting topoisomerase II. Not Sci Biol. 2025;17(3):12642. https://doi.org/10.55779/nsb17312642
17. Van Der Spoel D, Lindahl E, Hess B, Groenhof G, Mark AE, Berendsen HJC. GROMACS: Fast, flexible, and free. J Comput Chem. 2005;26(16):1701–18. https://doi.org/10.1002/jcc.20291
18. Zoete V, Cuendet MA, Grosdidier A, Michielin O. SwissParam: A fast force field generation tool for small organic molecules. J Comput Chem. 2011;32(11):2359–68. https://doi.org/10.1002/jcc.21816
19. Pettersen EF, Goddard TD, Huang CC, Couch GS, Greenblatt DM, Meng EC, et al. UCSF Chimera–A visualization system for exploratory research and analysis. J Comput Chem. 2004;25(13):1605–12. https://doi.org/10.1002/jcc.20084
20. Nguyen HD. Unveiling the anti-apoptotic mechanism of magnolialide as a colorectal cancer inhibitor via molecular modeling, ADMET, and MMGBSA analysis. Phys Chem Res. 2025;13(4):783–96.

https://doi.org/10.22036/pcr.2025.535946.2708
21. Pires DE, Blundell TL, Ascher DB. pkCSM: Predicting small-molecule pharmacokinetic and toxicity properties using graph-based signatures. J Med Chem. 2015;58(9):4066–72. https://doi.org/10.1021/acs.jmedchem.5b00104
22. Neese F. Software update: The ORCA program system–version 6.0. Wiley Interdiscip Rev Comput Mol Sci. 2025;15(2):e70019. https://doi.org/10.1002/wcms.70019
23. Knizia G, Klein JE. Electron flow in reaction mechanisms–revealed from first principles. Angew Chem Int Ed. 2015;54(18):5518–22. https://doi.org/10.1002/anie.201410637
24. Hanwell MD, Curtis DE, Lonie DC, Vandermeersch T, Zurek E, Hutchison GR. Avogadro: an advanced semantic chemical editor, visualization, and analysis platform. J Cheminform. 2012;4(1):17. https://doi.org/10.1186/1758-2946-4-17
25. Luo J, Xue ZQ, Liu WM, Wu JL, Yang ZQ. Koopmans' theorem for large molecular systems within density functional theory. J Phys Chem. A. 2006;110(43):12005–9. https://doi.org/10.1021/jp063669m
26. Das R, Vigneresse J-L, Chattaraj PK. Chemical reactivity through structure-stability landscape. Int J Quantum Chem. 2014;114(21):1421–9. https://doi.org/10.1002/qua.24706
27. Bell EW, Zhang Y. DockRMSD: An open-source tool for atom mapping and RMSD calculation of symmetric molecules through graph isomorphism. J Cheminform. 2019;11(1):40. https://doi.org/10.1186/s13321-019-0362-7
28. Hollingsworth SA, Dror RO. Molecular dynamics simulation for all. Neuron 2018;99(6):1129-43. https://doi.org/10.1016/j.neuron.2018.08.011
29. Zhao S, Ma S, Zhang Y, Gao M, Luo Z, Cai S. Combining molecular docking and molecular dynamics simulation to discover four novel umami peptides from tuna skeletal myosin with sensory evaluation validation. Food Chem. 2024;433:137331. https://doi.org/10.1016/j.foodchem.2023.137331
30. Salmaso V, Moro S. Bridging molecular docking to molecular dynamics in exploring ligand-protein recognition process: An overview. Front Pharmacol. 2018;9:923. https://doi.org/10.3389/fphar.2018.00923
31. Hosseini M, Fattahi A, Pakzadiyan A. Computational and experimental design of L-amino acid-based alternatives to ketorolac. Sci Rep. 2025;15(1):42161. https://doi.org/10.1038/s41598-025-26171-1
32. Schiffmann C, Sebastiani D. Hydrogen bond networks: Structure and dynamics via first-principles spectroscopy. Phys Status Solidi B. 2012;249(2):368–75. https://doi.org/10.1002/pssb.201100556
33. Wang E, Sun H, Wang J, Wang Z, Liu H, Zhang JZH, et al. End-point binding free energy calculation with MM/PBSA and MM/GBSA: Strategies and applications in drug design. Chem Rev. 2019;119(16):9478–508. https://doi.org/10.1021/acs.chemrev.9b00055
34. Ferreira LLG, Andricopulo AD. ADMET modeling approaches in drug discovery. Drug Discov Today. 2019;24(5):1157–65. https://doi.org/10.1016/j.drudis.2019.03.015
35. Chandrasekaran B, Abed SN, Al-Attraqchi O, Kuche K, Tekade RK. Computer-aided prediction of pharmacokinetic (ADMET) properties. In: Tekade RK, editor. Dosage Form Design Parameters. Volume II. Oxford: Academic Press; 2018 p. 731–55. https://doi.org/10.1016/B978-0-12-814421-3.00021-X
36. Nguyen HD. DFT and molecular modelling reveal the mechanism of action of selected alkaloids as anti-colorectal cancer agents targeting topoisomerase II. Not Sci Biol. 2025;17(3):12642. https://doi.org/10.55779/nsb17312642
37. Zhao M, Ma J, Li M, Zhang Y, Jiang B, Zhao X, et al. Cytochrome P450 enzymes and drug metabolism in humans. Int J Mol Sci. 2021;22(23):12808. https://doi.org/10.3390/ijms222312808

КОМП'ЮТЕРНЕ МОДЕЛЮВАННЯ ОКРЕМИХ ФІТОХІМІЧНИХ РЕЧОВИН, ОТРИМАНИХ З *Reevesia formosana*: МЕХАНІСТИЧНИЙ АНАЛІЗ ЇХНЬОГО ПОТЕНЦІАЛУ У БОРОТЬБІ З РАКОМ ЛЕГЕНІВ

Хунг Дук Нгуєн
Факультет біології, Педагогічний університет Тай Нгуєна, 24000, Тай Нгуєн, В'єтнам
e-mail: hungnd@tnue.edu.vn

Надійшла до редакції 10 грудня 2025 р. Переглянута 07 березня 2026 р.
Прийнята до друку 16 березня 2026 р. Опублікована 25 червня 2026 р.

Актуальність. Рак легенів залишається провідною причиною смертності від онкологічних захворювань, а порушення апоптозу, опосередковане антиапоптотичними білками сімейства Bcl-2, сприяє персистенції захворювання та резистентності до лікування. Фітохімічні сполуки з *Reevesia formosana*, як повідомляється, виявляють протипухлинну активність щодо недрібноклітинного раку легенів (NSCLC), проте механізми дії на рівні мішеней досі не до кінця з'ясовані.
Мета: визначити пріоритети фітохімічних речовин Reevesia formosana як ймовірних інгібіторів Bcl-2 (PDB ID: 6GL8) та отримати механістичне розуміння за допомогою багатомасштабних обчислень.

Матеріали та методи: Шість фітохімічних сполук та еталонний препарат Tivantinib були піддані докінгу до білка 6GL8, а найкращий кандидат (CPD1) було оцінено за допомогою моделювання методом молекулярної динаміки тривалістю 100 нс у порівнянні з Tivantinib. Вільні енергії зв'язування MMGBSA були обчислені на основі 125 знімків, зроблених у проміжку від 20 до 100 нс. Властивості ADMET було передбачено за допомогою pkCSM. Дескриптори граничних орбіталей та глобальної реакційної здатності були отримані за допомогою DFT.

Результати: За результатами докінгу CPD1 посів перше місце (-10,15 ккал/моль) порівняно з Tivantinib (-8,83 ккал/моль), демонструючи водневі зв’язки з Tyr108 та Arg129, а також високий ступінь комплементарності кишень. Траєкторії MD вказували на більш обмежений комплекс CPD1-6GL8 (RMSD переважно 0,18–0,22 нм) порівняно з Tivantinib-6GL8 (0,21–0,26 нм, інколи 0,27–0,28 нм), з порівнянною компактністю (Rg 1,44 нм) та обмеженою SASA. Кількість водневих зв'язків підтверджувала переривчасте полярне закріплення для CPD1 (0–3) та вищу ранню вибірку для Tivantinib. MMGBSA віддавала перевагу CPD1 (ΔTOTAL -32,87 ± 4,28 ккал/моль) над Tivantinib (-17,27 ± 2,81 ккал/моль), що підтверджувалося сильнішим ΔVDWAALS (-40,76 проти -31,34 ккал/моль) та меншим ΔG_SOLV (20,28 проти 24,14 ккал/моль). Прогноз ADMET вказав на високу кишкову абсорбцію з обмеженою розчинністю, обмежену проникність через ГЕБ/ЦНС, менше ознак інгібування CYP та відсутність попередження про гепатотоксичність для CPD1, тоді як інгібування hERG II було відзначено для обох лігандів. DFT показав подібний EHOMO (eV), але вужчий ΔE (eV) та вищий ω (eV) для CPD1, ніж для Tivantinib.

Висновки: Інтегроване моделювання надає пріоритет CPD1 як скафолду, що націлений на Bcl-2, для досліджень, пов’язаних із раком легенів, підтримуючи оптимізацію на основі структури та експериментальну верифікацію.

КЛЮЧОВІ СЛОВА: ADMET; антиапоптоз; Bcl-2; MMGBSA; молекулярне моделювання; Reevesia formosana.